

VOLUME 280 (2005) PAGES 12799–12809

Interaction of the mammalian endosomal sorting complex required for transport (ESCRT) III protein hSnf7-1 with itself, membranes, and the AAA⁺ ATPase SKD1.

Yuan Lin, Lisa A. Kimpler, Teresa V. Naismith, Joshua M. Lauer, and Phyllis I. Hanson

The plasmid used to express FLAG-hSnf7N (residues 1–116) in this paper had an unintended missense mutation changing serine at residue 2 to cysteine. We found that this cysteine was palmitoylated. Changing it back to serine decreased the amount of hSnf7N associated with membranes from all for the mutant fragment containing cysteine to approximately half for the wild-type fragment containing serine. The images of FLAG-hSnf7N in Figs. 7B and 8 represent average cells expressing mutant (Cys-2) hSnf7N, whereas for wild-type (Ser-2) hSnf7N, these images correspond to cells expressing high levels of protein. All other plasmids are as indicated, and the conclusions of the paper remain unchanged.

VOLUME 280 (2005) PAGES 28382–28387

Role of the N-terminal domain of the human DMC1 protein in octamer formation and DNA binding.

Takashi Kinebuchi, Wataru Kagawa, Hitoshi Kurumizaka, and Shigeyuki Yokoyama

PAGE 28385:

Due to an inadvertent error, the wrong image was presented in Fig. 4C. Fig. 4C should appear as shown below. The figure legend and text remain unchanged.

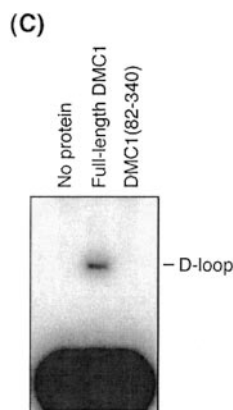


FIGURE 4C

VOLUME 281 (2006) PAGES 8888–8897

Dynamic changes in histone H3 lysine 9 methylations. IDENTIFICATION OF A MITOSIS-SPECIFIC FUNCTION FOR DYNAMIC METHYLATION IN CHROMOSOME CONGRESSION AND SEGREGATION.

Kirk J. McManus, Vincent L. Biron, Ryan Heit, D. Alan Underhill, and Michael J. Hendzel

The concentration of a drug that was employed, adenosine dialdehyde, was erroneously reported as 25 mM. The concentration that was employed was actually 250 μ M.

VOLUME 281 (2006) PAGES 23436–23444

Conditional deletion of hypothalamic Y2 receptors reverts gonadectomy-induced bone loss in adult mice.

Susan J. Allison, Paul Baldock, Amanda Sainsbury, Ronaldo Enriquez, Nicola J. Lee, En-Ju Deborah Lin, Matthias Klugmann, Matthew During, John A. Eisman, Mei Li, Lydia C. Pan, Herbert Herzog, and Edith M. Gardiner

PAGE 23436:

Dr. Klugmann's name was misspelled in the author line. The correct spelling is shown above.

VOLUME 281 (2006) PAGES 31553–31561

The first structure from the SOUL/HBP family of heme-binding proteins, murine P22HBP.

Jorge S. Dias, Anjos L. Macedo, Gloria C. Ferreira, Francis C. Peterson, Brian F. Volkman, and Brian J. Goodfellow

PAGE 31554:

Column 2, first line: The concentrations should read "(4.0 μ M) or hemin (3.5 μ M). . ."

We suggest that subscribers photocopy these corrections and insert the photocopies in the original publication at the location of the original article. Authors are urged to introduce these corrections into any reprints they distribute. Secondary (abstract) services are urged to carry notice of these corrections as prominently as they carried the original abstracts.

PTP-PEST couples membrane protrusion and tail retraction via VAV2 and p190RhoGAP.

Sarita K. Sastry, Zenon Rajfur, Betty P. Liu, Jean-Francois Cote, Michel L. Tremblay, and Keith Burridge

PAGE 11632:

In Fig. 5, *panel D* was inadvertently omitted and is shown below. The figure legend is correct as it appears.

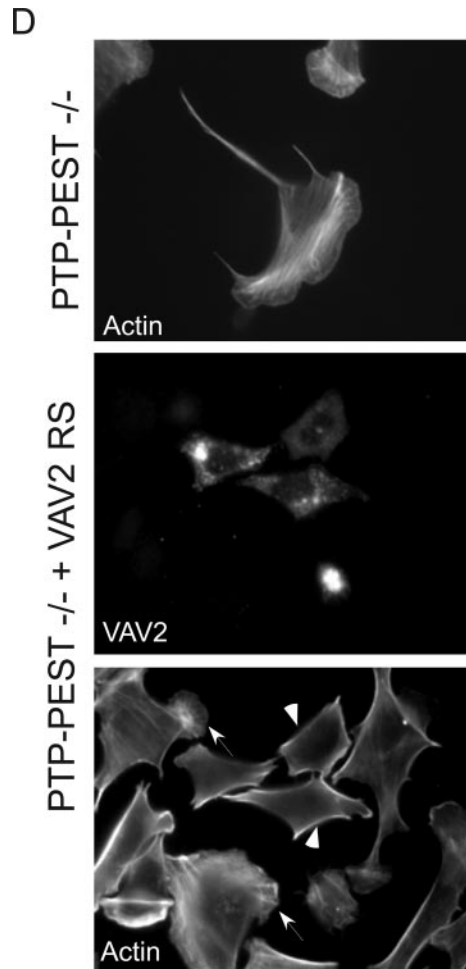


FIGURE 5

Correction of pulmonary abnormalities in *Sftpd*^{-/-} mice requires the collagenous domain of surfactant protein D.

Paul S. Kingma, Liqian Zhang, Machiko Ikegami, Kevan Hartshorn, Francis X. McCormack, and Jeffrey A. Whitsett

PAGE 24501:

Fig. 5: An incorrect image was used for the *panel A inset*. The correct image is shown below.

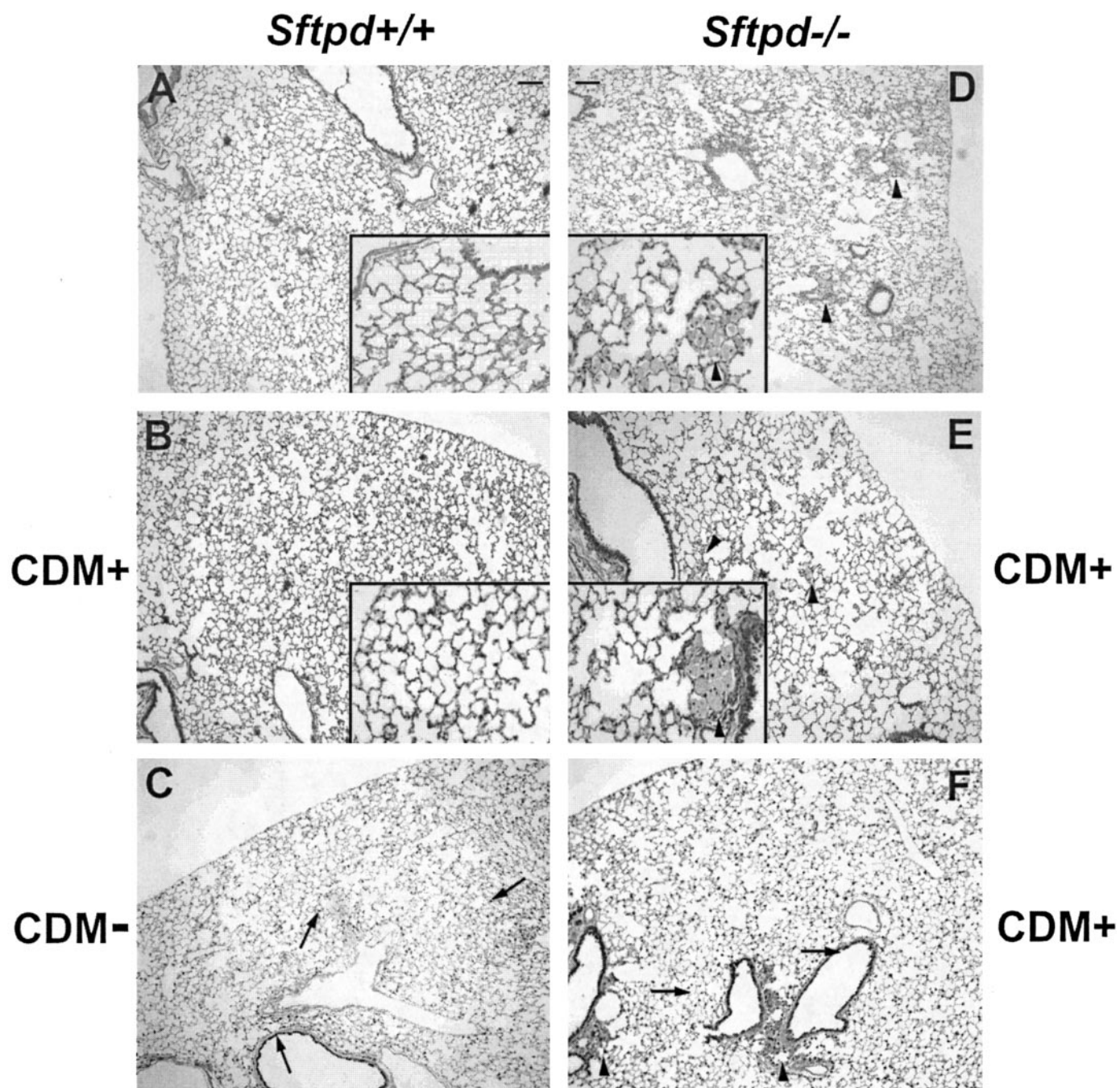


FIGURE 5

The First Structure from the SOUL/HBP Family of Heme-binding Proteins, Murine P22HBP*

Received for publication, June 22, 2006, and in revised form, August 10, 2006 Published, JBC Papers in Press, August 10, 2006, DOI 10.1074/jbc.M605988200

Jorge S. Dias[‡], Anjos L. Macedo[‡], Gloria C. Ferreira[§], Francis C. Peterson[¶], Brian F. Volkman[¶], and Brian J. Goodfellow^{||}

From the [‡]Rede de Química e Tecnologia, Centro de Química Fina e Biotecnologia, Departamento de Química, Faculdade de Ciências e Tecnologia, Universidade Nova de Lisboa, 2829-516 Caparica, Portugal, the [§]Department of Molecular Medicine, College of Medicine, University of South Florida, Tampa, Florida 33612-4799, the [¶]Department of Biochemistry, Medical College of Wisconsin, Milwaukee, Wisconsin 53226, and ^{||}Centro de Investigação em Materiais Cerâmicos e Compósitos, Departamento de Química, Universidade de Aveiro, 3810-193 Aveiro, Portugal

Murine p22HBP, a 22-kDa monomer originally identified as a cytosolic heme-binding protein ubiquitously expressed in various tissues, has 27% sequence identity to murine SOUL, a heme-binding hexamer specifically expressed in the retina. In contrast to murine SOUL, which binds one heme per subunit via coordination of the Fe(III)-heme to a histidine, murine p22HBP binds one heme molecule per subunit with no specific axial ligand coordination of the Fe(III)-heme. Using intrinsic protein fluorescence quenching, the values for the dissociation constants of p22HBP for hemin and protoporphyrin-IX were determined to be in the low nanomolar range. The three-dimensional structure of murine p22HBP, the first for a protein from the SOUL/HBP family, was determined by NMR methods to consist of a 9-stranded distorted β -barrel flanked by two long α -helices. Although homologous domains have been found in three bacterial proteins, two of which are transcription factors, the fold determined for p22HBP corresponds to a novel α plus β fold in a eukaryotic protein. Chemical shift mapping localized the tetrapyrrole binding site to a hydrophobic cleft formed by residues from helix α_A and an extended loop. In an attempt to assess the structural basis for tetrapyrrole binding in the SOUL/HBP family, models for the p22HBP-protoporphyrin-IX complex and the SOUL protein were generated by manual docking and automated methods.

Heme synthesis occurs mainly in erythroid cells (~85%) and hepatocytes, although heme is synthesized in virtually all tissues. In hepatocytes, heme is required for incorporation into cytochromes, in particular, the P450 class of cytochromes that are important for detoxification. Numerous other cytochromes

of the oxidative-phosphorylation pathway also contain heme. 5-Aminolevulinic acid synthase (ALAS)² catalyzes the first, and rate-limiting, step in hepatic heme biosynthesis. Hemin, the Fe(III) oxidation product of heme, acts as a feedback inhibitor of ALAS as well as an inhibitor of mitochondrial transport of ALAS; via an interaction with the ALAS presequence (1), hemin prevents ALAS from reaching its mitochondrial, mature, active form (2).

Because porphyrins and metallated porphyrins (*e.g.* heme) are extremely reactive and poorly soluble in aqueous solution under physiological conditions, it was hypothesized that one or more intracellular heme-binding proteins act as a buffer during induced heme synthesis (3). p22HBP, a 22-kDa protein, was first purified from mouse liver cell extracts and characterized as a cytosolic, heme-binding protein by Taketani *et al.* in 1998 (4). Blackmon *et al.* (3) subsequently determined that p22HBP binds other tetrapyrroles in addition to hemin, although its functional role in the cell remains unknown. However, a recent proteomic study, involving metabolic labeling with ⁵⁹Fe-hemin of murine erythroleukemia cells induced to undergo differentiation, demonstrated that p22HBP is a component in one of the four identified multiprotein complexes related to hemoglobin biosynthesis (5). The investigators suggested that p22HBP could either function as a heme transporter or chaperone for heme insertion into hemoglobin or as a mediator of import of coproporphyrinogen into mitochondria (5).

An acetylated N-terminal fragment of p22HBP (residues 1–21) has also been recently purified from porcine spleen extract on the basis of potent chemoattractant activity. This peptide, named F2L, selectively recruits leukocytes by activating the formyl peptide receptor-like 2 (FPRL2), a G protein-coupled receptor expressed specifically on monocytes and dendritic cells. Until this discovery, FPRL2 was an orphan receptor in the family of formyl peptide receptors that typically bind bacterially secreted peptide ligands. F2L is a potent FPRL2 agonist with ~7 nM binding affinity (6). Although acetylation of the p22HBP N-terminal Met residue was not essential for F2L

* This work was supported by the Fundação para a Ciência e Tecnologia, Programa Operacional Ciência, Tecnologia, Inovação (POCTI), and Fundo Europeu de Desenvolvimento Regional in Portugal (Grant SFRH/BD/3091/2000 to J. S. D. and Grant POCTI/BME/39184/2001 to B. J. G. and A. L. M.) and National Institutes of Health Grants GM64598 (to B. F. V.) and DK63191 (to G. C. F.). The costs of publication of this article were defrayed in part by the payment of page charges. This article must therefore be hereby marked "advertisement" in accordance with 18 U.S.C. Section 1734 solely to indicate this fact.

The atomic coordinates and structure factors (code 2GOV) have been deposited in the Protein Data Bank, Research Collaboratory for Structural Bioinformatics, Rutgers University, New Brunswick, NJ (<http://www.rcsb.org/>).

¹ To whom correspondence should be addressed. Tel.: 351-234-401-506; Fax: 351-234-370-084; E-mail: brian.goodfellow@dq.ua.pt.

² The abbreviations used are: ALAS, 5-aminolevulinic acid synthase; PPIX, protoporphyrin-IX; HSQC, heteronuclear single quantum coherence; TROSY, transverse relaxation optimized spectroscopy; TOCSY, total correlation spectroscopy; NOE, nuclear Overhauser enhancement; 2D, 3D, two- and three-dimensional; FPRL2, formyl peptide receptor-like 2; NOESY, nuclear Overhauser effect spectroscopy; r.m.s.d., root mean square deviation.

Solution Structure of p22HBP

activity, it is not known whether full-length p22HBP protein can also bind and activate FPRL2. Whether the intracellular heme binding and immune signaling activities attributed to p22HBP are interrelated also remains to be seen.

p22HBP is part of an evolutionarily conserved heme-binding protein family with at least two distinct members. The SOUL protein is expressed in retina and pineal gland in the domestic chicken and solely in the retina in the murine form (7). Murine SOUL has 27% sequence identity to murine p22HBP and also binds heme. However, although p22HBP is a monomer that appears to bind one heme molecule per subunit with no specific axial ligand coordination of the Fe(III) heme, murine SOUL is a hexameric protein that binds one heme per subunit via coordination of the Fe(III) heme to a histidine side chain (7, 8).

No structural information exists for p22HBP or SOUL, and sequence analysis has identified no obvious similarity to known protein folds. To further understand the structural and molecular basis for their functional roles, we determined the first structure of a protein from the SOUL/HBP family, p22HBP, and monitored heme binding by NMR spectroscopy. The p22HBP structure consists of a 9-stranded twisted β -barrel flanked by two α -helices. Dissociation constants for the p22HBP-hemin and p22HBP-PPIX complexes were determined by fluorescence quenching to be in the low nanomolar range. To locate the tetrapyrrole binding site, chemical shift perturbations arising from the addition of hemin and protoporphyrin-IX (PPIX) were mapped to the p22HBP structure. The tetrapyrrole ring interacts with a hydrophobic groove formed by the α_A helix and the β_8 - β_9 loop. From sequence alignments and homology modeling, we conclude that, although p22HBP and SOUL share what is likely to be a conserved tertiary fold, they bind heme at different sites within this fold.

MATERIALS AND METHODS

Protein Production—p22HBP was overexpressed and purified as described previously (9). As murine p22HBP was originally purified in an N-terminally truncated form (4), the protein used for the NMR measurements corresponded to residues 7–190 of the murine p22HBP gene product plus an N-terminal sequence (MKQSTHHHHHH-) introduced for affinity purification. Protein purity was assessed by SDS-PAGE, and concentrations were determined by bicinchoninic acid assay (10).

Preparation of Tetrapyrrole Solutions—Hemin and PPIX (Frontier Scientific) were used without further purification. Due to their poor solubility in acidic and neutral pH, tetrapyrroles were initially dissolved in ammonia followed by dilution in water. After addition of a surfactant, Tween 80 (1.5% v/v), the pH was adjusted to 8.0 with KH_2PO_4 .

Tryptophan Fluorescence Quenching—All fluorescence measurements were performed using a Photon Technology International QM-4 spectrofluorometer at 303 K. The protein sample used for the fluorescence quenching measurements was prepared by dilution from a stock solution at 1 mM with 50 mM phosphate buffer at pH 8.0. The protein concentration used in the titration was estimated by UV spectroscopy (an ϵ_{280} of $36900 \text{ M}^{-1} \text{ cm}^{-1}$ was used) to be 7.5 nM. Protoporphyrin-IX

(4.0 mM) or hemin (3.5 mM) was added in aliquots of $2 \mu\text{l}$ (36 μl total) to 1 ml of the protein solution. After sample equilibration (3 min), three emission scans from 300 to 400 nm with excitation at 295 nm were recorded and averaged. Emission spectra were baseline corrected and smoothed using the FeliX32 software (Photon Technology International, Inc.). Dissociation constants (K_d) were obtained by nonlinear fitting of the emission maxima (y) as a function of tetrapyrrole concentration (x) using a binding model that accounts for ligand depletion at high receptor concentration (11),

$$y = \frac{I_0 - (I_0 - I_{\text{inf}})}{2[\text{hbp}]} \left[(K_d + [\text{hbp}] + x) - \sqrt{(K_d + [\text{hbp}] + x)^2 - 4[\text{hbp}]x} \right] \quad (\text{Eq. 1})$$

where I_0 and I_{inf} are emission intensities at 0 and saturating concentrations of tetrapyrrole, respectively, and $[\text{hbp}]$ is the protein concentration. Uncertainties associated with the determinations were obtained from replicate measurements.

NMR Spectroscopy—NMR spectra were acquired at 30 °C on a Bruker DRX-600 spectrometer equipped with a 5-mm inverse triple-resonance cryoprobe with a z-axis gradient coil. Protein samples for structure determination by NMR contained [$\text{U-}^{15}\text{N}$]- or [$\text{U-}^{15}\text{N},^{13}\text{C}$]p22HBP (0.5–1 mM), 5% D_2O , and 50 mM potassium phosphate buffer at pH 8.0. At pH 7.0 the protein precipitated after a few hours. Backbone ^1H , ^{13}C , and ^{15}N resonances were assigned using a combination of automated and manual methods with data from the following experiments: 2D ^{15}N HSQC, 2D TROSY, 3D TROSY-HNCO, TROSY-HN(CA)CO, TROSY-HNCA, TROSY-HN(CO)CA, TROSY-HNCACB, TROSY-HN(CO)CACB, ^{15}N -edited NOESY-HSQC (mixing time, 60 ms), and ^{15}N -edited TOCSY-HSQC (mixing time, 43.2 ms) spectra. Aliphatic side-chain resonances were assigned manually from a 3D HCCH-TOCSY spectrum (mixing time, 16.3 ms), and aromatic resonance assignments were obtained from a ^{13}C -edited NOESY-HSQC (mixing time, 80 ms) spectrum centered in the aromatic region. Spectra were processed and analyzed using NMRPipe (12), CARA (13), and XEASY (14) software. Chemical shifts were referenced, either directly or indirectly, to 2,2-dimethyl-2-silapentane-5-sulfonate sodium salt at 0 ppm (15).

A series of 2D and 3D spectra, including $^1\text{H},^{15}\text{N}$ -TROSY, 3D TROSY-HNCO, and TROSY-HNCA were acquired on p22HBP in the presence of hemin or PPIX. NMR samples of complexes were prepared in 150 mM potassium phosphate buffer at pH 8.0, 1.5% Tween 80 and 5% D_2O .

Structure Determination—Using the software program TALOS (16), backbone ϕ and ψ angles were initially derived from $^1\text{H}^\alpha$, $^{15}\text{N}^{\text{H}}$, $^{13}\text{C}^\alpha$, $^{13}\text{C}^\beta$, and $^{13}\text{C}'$ chemical shifts. Distance constraints were obtained from 3D ^{15}N -edited NOESY-HSQC, ^{13}C (aromatic)-edited NOESY-HSQC, and ^{13}C -edited NOESY-HSQC spectra. Structures were generated in an automated manner using the NOEASSIGN module of the torsion angle dynamics program CYANA 2.1 (17), followed by manual refinement of the NOE assignments to eliminate consistent

violations. The 20 CYANA conformers with the lowest target function were subjected to a molecular dynamics protocol in explicit solvent (18) using XPLOR-NIH (19). Procheck-NMR (20) and WHATCHECK were used to validate the final family of 20 NMR structures, and the statistics for these are listed in Table 1. The coordinates and experimental constraints have been deposited in the Protein Data Bank (PDB) entry 2GOV.

Bioinformatic Analysis—Amino acid sequence searches were performed using the NCBI BLAST server (21). Structural homology searches were performed using the VAST (22) and FATCAT (23) servers. Protein electrostatic potential surfaces were calculated using APBS (24). Input structure files for the APBS program were prepared using pdb2pqr (25). The amber force field was used in all cases, and the pH was set to 8.0. Homology modeling was performed using MODELLER8 ver-

sion 2 (26). The target sequences were initially aligned with the representative 2GOV structure and then five models were built. Discrete optimized protein energy scores were used to assess the quality of the resulting models.

RESULTS

Tetrapyrrole-p22HBP Binding Affinity—p22HBP was identified as a protein that binds both hemin and PPIX, but K_d values in both the nanomolar and micromolar ranges have been reported (3,4,8). In anticipation of structural studies of p22HBP complexes, we sought to resolve this discrepancy. We confirmed that recombinant p22HBP binds to both PPIX and hemin by comparing the intrinsic tryptophan fluorescence spectrum of the protein in the presence and absence of tetrapyrrole. As previously described (3), each ligand caused efficient quenching of the p22HBP tryptophan emission spectrum (data not shown). By nonlinear fitting of fluorescence quenching at 340 nm as a function of tetrapyrrole concentration (Fig. 1), we obtained K_d values of 0.5 and 3 nM for the PPIX and hemin complexes, respectively.

Structure of p22HBP—Having established the hemin and PPIX binding properties of recombinant p22HBP, we determined the 3D structure of free p22HBP by NMR spectroscopy. Chemical shift assignments for p22HBP were obtained by standard triple-resonance methods, as reported previously (BioMagResBank entry 6620) (9). Under the conditions used (30 °C and pH 8.0) some solvent-exposed amide resonances in the flexible N terminus and loop residues 173–180 were undetected due to exchange broadening. Outside these regions, ^1H , ^{15}N , and ^{13}C assignments were >90% complete. A total of 1851 NOE distance constraints and 276 dihedral angle constraints were used to define the final NMR ensemble (Fig. 2*a*). Backbone atomic r.m.s.d. values are ~0.6 Å in regions of secondary structure, and 0.82 Å for the entire protein, excluding the disordered N terminus and loop residues 173–180. Ramachandran statis-

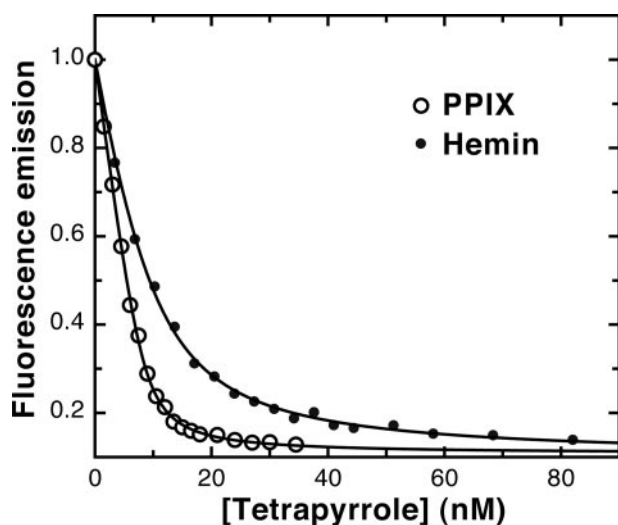


FIGURE 1. **Tetrapyrrole binding affinity.** Intrinsic tryptophan fluorescence emission intensity (at 340 nm with excitation at 295 nm) for p22HBP is plotted as a function of increasing PPIX or hemin concentration. Each titration dataset was fitted to Equation 1 to obtain K_d values of 0.5 and 3 nM for PPIX and hemin, respectively.

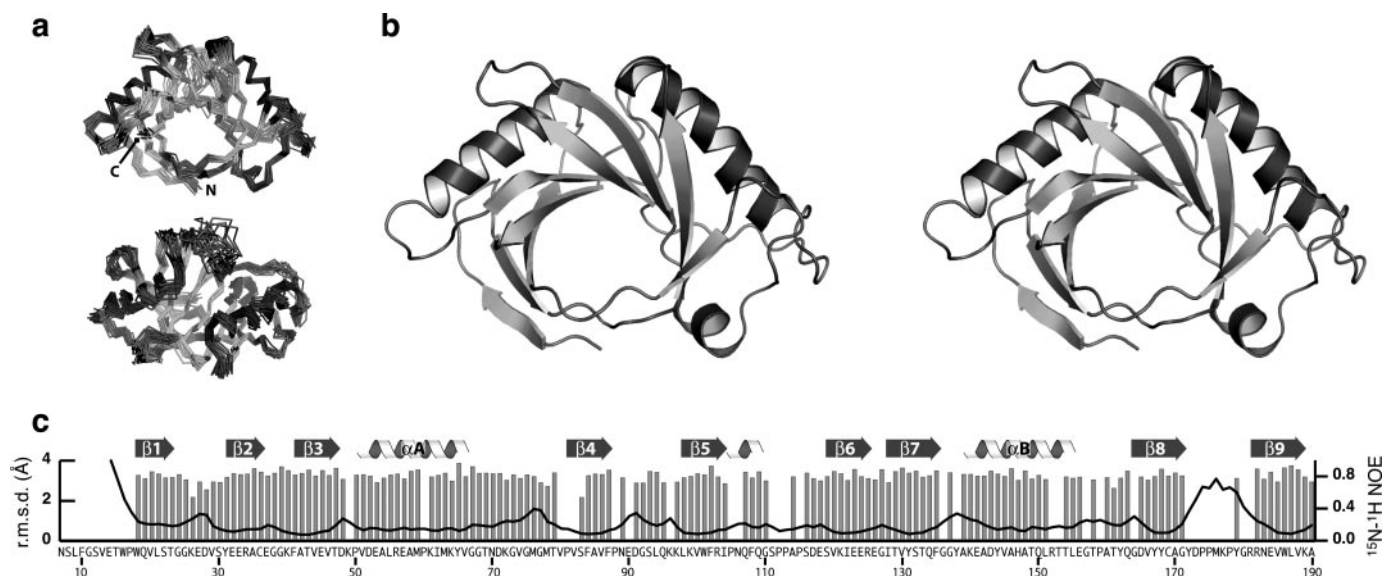


FIGURE 2. **The NMR solution structure of murine p22HBP.** *a*, ensemble of 20 p22HBP conformers. Residues 7–16 are omitted for clarity. *b*, stereoview of the p22HBP structure in ribbon representation. *c*, heteronuclear ^{15}N - ^1H NOE values (gray bars) and backbone atomic r.m.s.d. values (black line) are plotted as a function of the p22HBP sequence.

TABLE 1
Statistics for the ensemble of 20 p22HBP conformers

Experimental constraints	
Non-redundant distance constraints (total)	1851
Long	778
Medium ($1 < (i - j) \leq 5$)	276
Sequential ($(i - j) = 1$)	425
Intraresidue ($i = j$)	372
Dihedral angle constraints (ϕ and ψ)	276
Average atomic r.m.s.d. to the mean structure (Å)	
Backbone (C α , C', N) ^a	0.82 \pm 0.15
Heavy atoms	1.28 \pm 0.14
Deviations from idealized covalent geometry	
Bond (Å)	0.015
Angles (°)	1.3
WHATCHECK quality indicators	
Z-score	-1.51 \pm 0.18
r.m.s. Z-score	
Bond lengths	0.79 \pm 0.02
Bond angles	0.67 \pm 0.02
Bumps	0 \pm 0
Constraint violations	
NOE distance (violations > 0.5 Å)	0 \pm 0
NOE distance r.m.s.d. (Å)	0.017 \pm 0.001
Dihedral angle (violations > 5°)	0.2 \pm 0.5
Dihedral angle r.m.s.d. (°)	0.83 \pm 0.08
Ramachandran statistics (% of all residues)	
Most favored	91.0 \pm 1.9
Additionally allowed	7.0 \pm 1.7
Generously allowed	0.9 \pm 0.8
Disallowed	1.1 \pm 0.6

^a N-terminal residues 7–17 and the disordered loop 172–180 were excluded from the r.m.s.d. calculations owing to dynamic disorder in these segments.

tics and other validation criteria (Table 1) indicate that the determination of structure is of high quality.

The p22HBP structure consists of a central core containing a nine-stranded antiparallel β -sheet arranged in a distorted barrel, flanked by two α -helices (Fig. 2b). As noted previously (27), this fold topology displays pseudo 2-fold symmetry suggestive of an ancestral gene-duplication event. Each helix packs against a four-stranded sheet in the same manner, such that the β_2 - β_3 - α_A - β_4 - β_5 subdomain (residues 21–105) is equivalent to the β_6 - β_7 - α_B - β_8 - β_9 subdomain (residues 114–190). The p22HBP subdomains were aligned using FATCAT (23) with an r.m.s.d. of 3.2 Å over 72 positions, but despite the clear pseudo-dyad structural similarity, their sequences are only 8% identical.

Overall, the p22HBP structure is well ordered, as reflected in uniformly high ¹⁵N-¹H heteronuclear NOE values (Fig. 2c). Aside from the unstructured N terminus, only residues 173–180 display high r.m.s.d. values. This loop may be dynamically disordered, but NOE values could not be measured for prolines and other unobserved NH signals in this region. However, an NOE value of 0.8 for Tyr-179 suggests this portion of the backbone is not dynamically disordered on the picosecond-nanosecond timescales reported by the ¹H-¹⁵N NOE. Accordingly, conformational flexibility on slower timescales (e.g. millisecond-microsecond) cannot be ruled out without further measurements.

The center of the p22HBP β -barrel is predominantly hydrophobic and contains a number of aromatic side chains. Likewise, the packing of the two long helices against the β -sheet is typically stabilized by hydrophobic side-chain interactions. Beyond the extensive backbone secondary structure interactions, one example of stabilizing side-chain hydrogen bonding stands out. The side chain of Asn-70 participates in three dif-

ferent hydrogen bonds, with the carbonyl of Tyr-65 and the backbone amide and carbonyl of Gly-74. This structure helps to define a tight turn in residues 70–73, which in turn packs on the surface of the structure against an extended proline-rich region from residues 112 to 115.

Structural Homologs of p22HBP—Searches for structures similar to p22HBP identified three proteins with domains that share a common α plus β fold: SbmC protein from *Escherichia coli* (27), the C-terminal domain of the *E. coli* transcription factor Rob (28), and the C-terminal multidrug-binding domain of transcription activator BmrR from *B. subtilis* (29, 30). A structure-based sequence alignment is shown in Fig. 3a. SbmC matches p22HBP with 8.6% sequence identity and a backbone r.m.s.d. of 3.0 Å, whereas the corresponding domains from Rob and BmrR each aligned to the p22HBP structure with an r.m.s.d. of 3.2 Å and sequence identities of 7.6 and 7.2%, respectively.

None of the identified structural homologs have been reported to bind tetrapyrroles. However, because each of these proteins displays the same overall fold as p22HBP (Fig. 3b), their active sites or interaction surfaces might also correspond to functional sites used by the heme-binding protein. SbmC, also known as gyrase inhibitory protein, has no identified binding partners or active site (27). Likewise, while the C-terminal domain of Rob is hypothesized to bind an effector molecule that regulates Rob transcriptional activity, no ligand has been identified (28).

Unlike the structural homologs of p22HBP, the BmrR C-terminal domain has a well defined small molecule binding site (29). BmrR regulates expression of the Bmr multidrug transporter in response to binding of Bmr substrate molecules, including rhodamine and tetraphenylphosphonium to the BmrR C-terminal domain. The crystal structure of BmrR bound to tetraphenylphosphonium revealed a dramatic conformational change upon ligand binding that involves unfolding of the α_B helix to reveal a buried glutamate side chain (29).

Electrostatic surfaces were calculated for p22HBP and the three structurally homologous proteins (Fig. 3c). An inspection of the electrostatic potential of the p22HBP surface revealed an hydrophobic patch/groove between helix α_A and a loop at 171–182 consisting of residues 55, 59, 62, 63, 66, 67, 76–78, 80, 82, 84, 100, 102, and 171. Of the p22HBP structural homologs, only the BmrR C-terminal domain in the absence of ligand (29, 30) displayed any significant hydrophobic exposure; this surface represents a likely point of entry to the tetraphenylphosphonium binding site.

The p22HBP Tetrapyrrole Binding Site—A series of 2D ¹H-¹⁵N TROSY spectra of 0.7 mM ¹⁵N-labeled p22HBP were collected to follow changes in chemical shifts upon the progressive addition of either heme or PPIX. However, in the presence of substoichiometric amounts of ligand two sets of TROSY signals were detected, corresponding to the free protein and the ligand-protein complex. At equimolar ratios of p22HBP and added ligand, the original signals corresponding to free protein were no longer visible, and ligand additions beyond one molar equivalent produced no further changes in the TROSY spectra. These observations are consistent with formation of a high affinity 1:1 complex with an off-rate corresponding to the slow

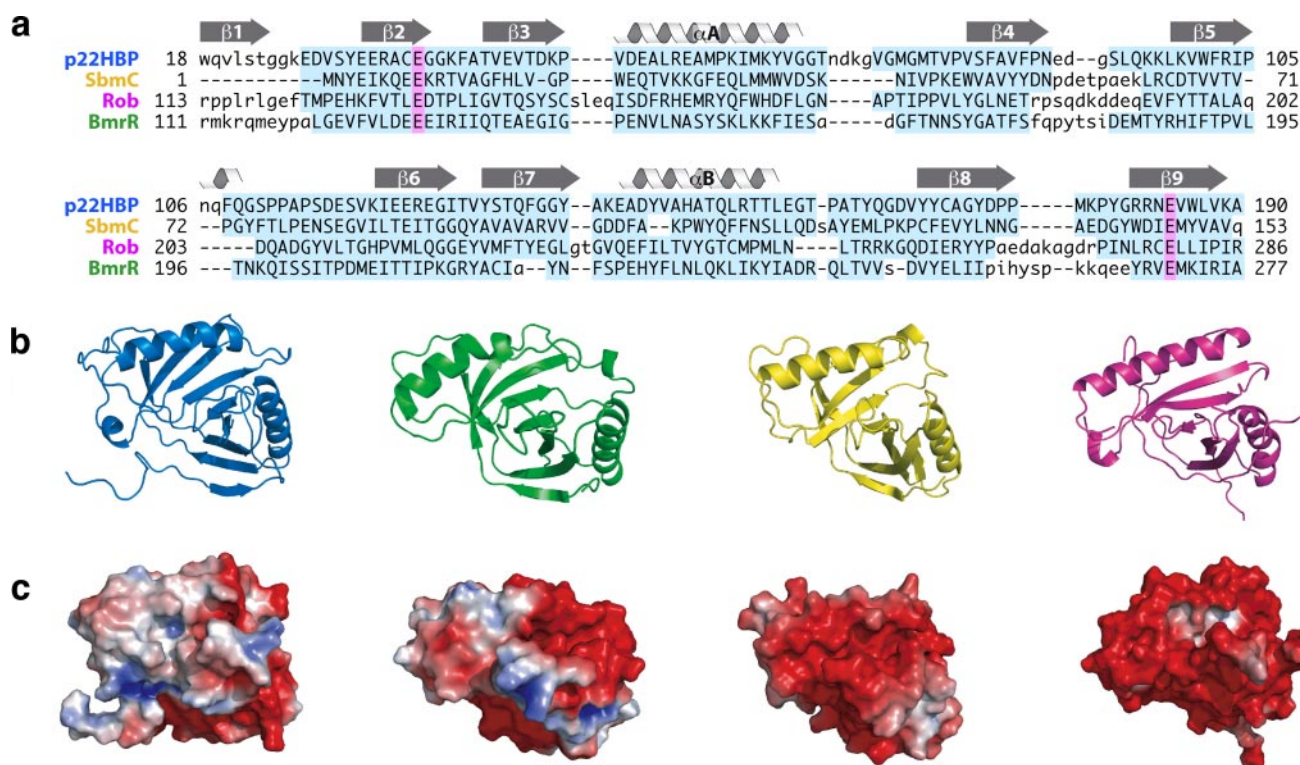


FIGURE 3. **Structural homologs of p22HBP.** *a*, structure-based sequence alignment (from FATCAT) for p22HBP, SbmC, Rob, and BmrR. The residues that were included in the FATCAT alignment are highlighted in *pale blue*, and the absolutely conserved residues are in *pink*. *b*, a representative conformer from the p22HBP ensemble is shown in *blue*, alongside the structures of SbmC (*gold*, PDB ID 1JYH), the C-terminal domain of Rob (*magenta*, PDB ID 1D5Y), and the BmrR multidrug binding domain (*green*, PDB ID 1R8E). *c*, electrostatic surface representations of p22HBP and its homologs, in the same orientation as in *b*.

exchange regime of the chemical shift time scale. Consequently, we collected additional 3D spectra on samples containing a slight excess of ligand (1.1:1, tetrapyrrole:p22HBP) to obtain the $^1\text{H}^N$, $^{13}\text{C}'$, $^{13}\text{C}^\alpha$, and $^{15}\text{N}^H$ chemical shifts of the complex. To ensure that correct assignments were obtained for residues exhibiting the largest shift perturbations, 3D TROSY-HNCA, TROSY-HNCO, and ^{15}N NOESY-HSQC spectra were recorded for each complex.

Heme ring current effects in protein NMR spectra have been studied for nearly 40 years (31), but to our knowledge no direct comparisons of shift perturbations from PPIX and hemin binding at the same site have been reported. Fig. 4*a* shows a superposition of portions of the TROSY spectra of p22HBP in the absence and presence of PPIX or hemin. For a majority of the shifted signals the free, PPIX- and hemin-bound signals display a linear relationship in the overlaid spectra, and the perturbation by hemin is typically greater than by PPIX. Some signals, particularly in the α_A helix (residues 55–64), and in residues 78, 83, 141, and 171–179, are absent in the hemin complex, presumably due to extreme broadening by the paramagnetic Fe(III) center. However, for residues that could be detected in all three spectra (free, PPIX, and hemin), chemical shift differences for p22HBP upon hemin binding are roughly twice the size of PPIX-induced perturbations (Fig. 4*b*). Presumably, this reflects an enhancement of the PPIX ring current field generated from electron withdrawal by the chelated iron in hemin. Aside from a difference in the magnitude of shift perturbations by PPIX and hemin, the patterns of chemical shift are

very similar, suggesting that the two ligands bind the same site in similar orientations.

The TROSY map of the PPIX-bound p22HBP also indicated that a number of shifted peaks near the binding site appear to become doubled in the presence of PPIX (this can be observed in the expansion of Fig. 4). This is due to the asymmetry of the PPIX ring and indicates that there are two possible (and from the roughly equal intensity of the cross-peaks, almost equally probable) binding orientations. The presence of peak doubling in the hemin-bound p22HBP TROSY spectrum is masked due to peaks from protons close to the binding site being either absent or broadened by the paramagnetism of the Fe(III) atom. By calculating the chemical shift differences, using the program SHIFTS-4.1 (32), for the PPIX ring in its binding position and for the ring flipped 180° about its pseudo 2-fold axis, it was possible to confirm that the magnitude of the chemical shifts (between ± 0.01 and 0.07 ppm) observed for the doubled peaks coincided with the calculated values.

PPIX-induced chemical shift differences were mapped to the p22HBP NMR structure (Fig. 4*c*) to identify the likely tetrapyrrole binding site. The largest perturbations cluster in a cleft bounded by the α_A helix and the β_8 – β_9 loop (residues 171–180). However, because the porphyrin can induce strong and highly directional ring current shifts, relatively distant parts of the structure are also affected. For example, residue Val-120 is on the opposite face of the protein that exhibits the largest cluster of shifts (the α_A helix) and is more than 9 Å from residue Met-63, which exhibits the largest shift upon PPIX binding. As

Solution Structure of p22HBP

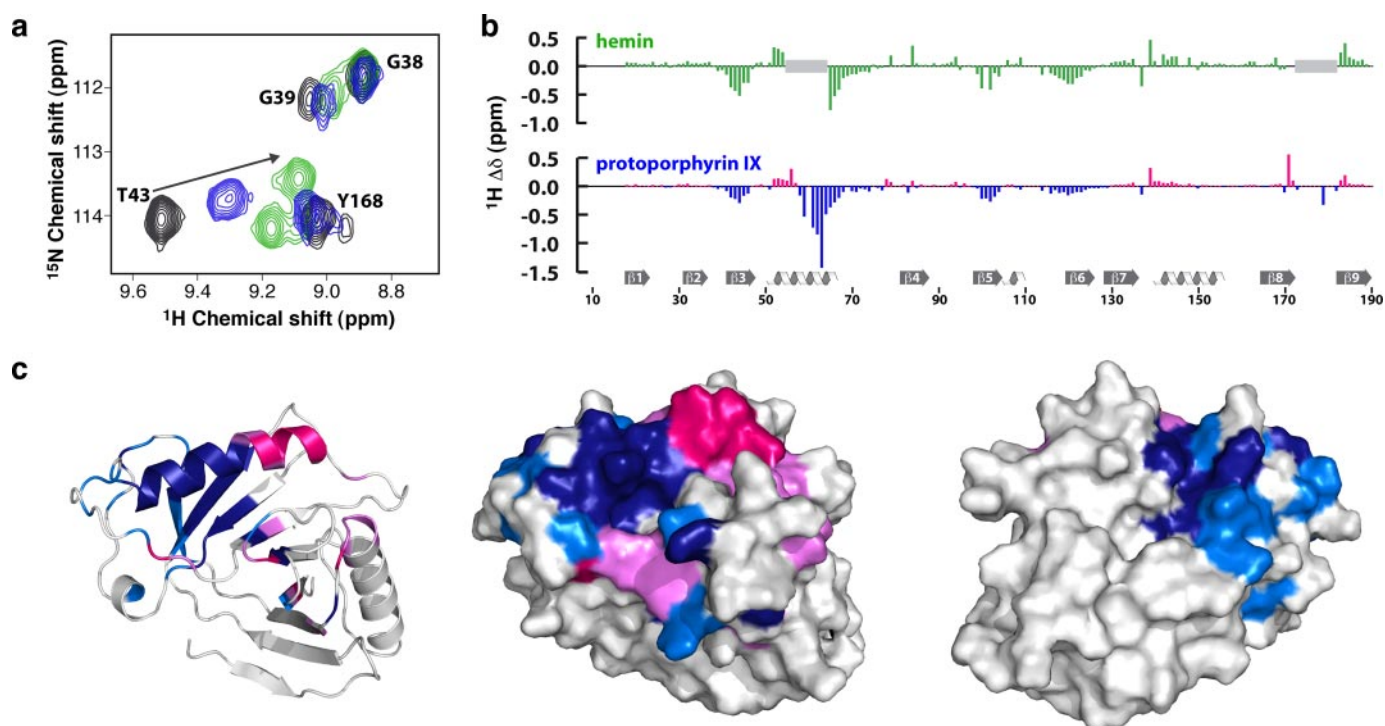


FIGURE 4. NMR titrations show that HBP binds heme and PPIX. *a*, overlay of a small region of the TROSY spectra for p22HBP (black contours), p22HBP-PPIX (blue contours), and p22HBP-hemin (green contours) showing shift perturbations upon tetrapyrrole binding. The p22HBP sample (without ligand) was prepared in solution conditions identical to the PPIX and hemin samples, including the presence of surfactant Tween-80. *b*, experimental chemical shift differences observed for murine p22HBP upon binding of hemin (upper) and PPIX (lower), plotted as a function of residue number with secondary structure elements indicated below. *c*, PPIX-induced shift perturbations displayed on the p22HBP structure. Small, negative shifts ($-0.05 > \Delta\delta > -0.1$ ppm) are shown in cyan, large negative shifts ($\Delta\delta < -0.1$) in blue, small, positive shifts ($0.05 < \Delta\delta < 0.1$ ppm) in violet, and large positive shifts ($\Delta\delta > 0.1$) in magenta. Ribbon (left) and surface (center) representations are shown in the same orientation, as well as a view of the surface rotated 180° about the vertical axis (right).

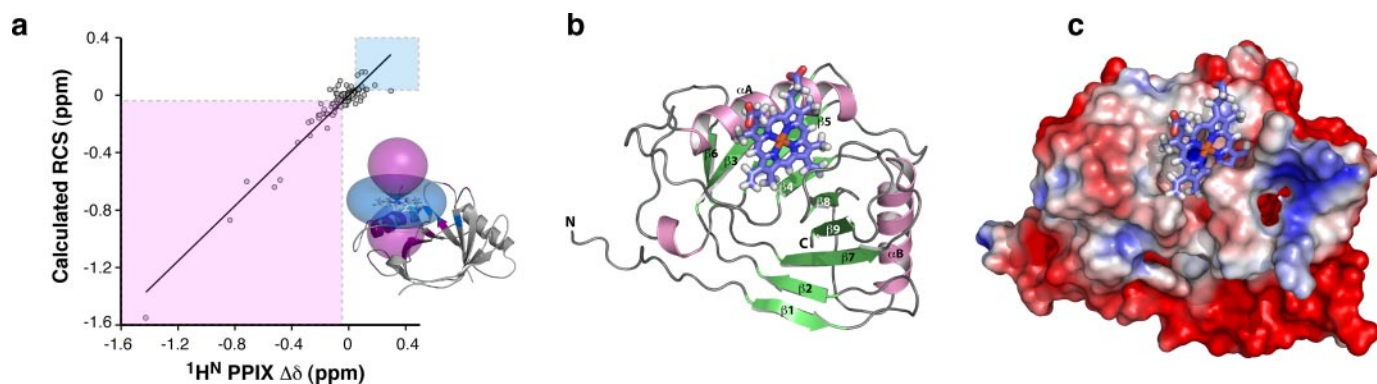


FIGURE 5. Model of the p22HBP-hemin complex. *a*, a correlation plot of the experimental and calculated chemical shift differences for p22HBP and PPIX bound p22HBP. The best-fit line is shown (slope = 0.96, intercept = 0.00, $R^2 = 0.90$). Residues 139, 171, and 179 exhibited significant deviations attributed to conformational changes upon ligand binding and were not used in the final analysis. The inset is a representation of the ring current chemical shift isosurface produced by a tetrapyrrole. *b*, the p22HBP structure with hemin docked at the binding site based on PPIX-induced ring current shifts. The binding location was determined by minimizing the differences between experimental chemical shift differences (Fig. 4*b*) and calculated PPIX ring current shifts. *c*, the p22HBP ligand binding site corresponds to the hydrophobic cleft identified in Fig. 3*c*. The electrostatic potential surface for p22HBP, calculated using APBS (20) (red = -3.0 eV, blue = $+3.0$ eV), is shown with docked hemin in the same orientation as in *b*.

discussed below, these long range chemical shift effects induced by PPIX can be exploited to gain a more detailed understanding of p22HBP ligand binding.

Model of the p22HBP-PPIX Complex—Chemical shift perturbations induced by binding of PPIX are probably dominated by ring current effects, which, like paramagnetic pseudocontact shifts (33), are rich with structural information on the distance and orientation relative to the origin of the shift perturbation. Similar to any dipolar interaction, the magnitude of the ring current shift falls off with r^{-3} . Depending on the location of a

nucleus relative to the plane of the PPIX, the ring current may either add to or subtract from the local magnetic field. The sign and magnitude of shift perturbations shown in Fig. 4*b* can therefore be used to define the location of the PPIX ligand bound to the p22HBP structure.

Ring currents in porphyrin systems induce shielding in nuclei above and below the plane of the porphyrin ring and deshielding around the “edge” of the ring (Fig. 5*a*). The largest shifts are observed for the residues around Met-63, and they are shielding in nature, thus the middle of the α_A helix must be above or below the



FIGURE 6. Sequence alignment for murine p22HBP and representative homologs. Initial alignment was performed using T-Coffee (36), with subsequent manual editing of N-terminal regions with low similarity. For each homolog, NCBI Entrez Protein accession numbers and the number of identical sequence positions aligned (using BLAST) to murine p22 HBP (Q9R257) are as follows: *Homo sapiens* heme-binding protein 1 (AAD32098), 164/189 (87%); *Xenopus laevis* MGC81367 protein (AAH68797), 106/189 (56%); *Danio rerio* hypothetical protein LOC393167 (NP_956492), 62/189 (32%); *Arabidopsis thaliana* At1g17100 (ABD43013), 43/153 (27%); *Rhodospseudomonas palustris* BisB18/SOUL heme-binding protein (YP_533080), 43/143, (30%); *H. sapiens* heme-binding protein 2/SOUL (Q9Y5Z4), 55/187 (29%); and *Mus musculus* heme-binding protein 2/SOUL (Q9WU63), 52/188 (27%).

plane, rather than in the same plane as the PPIX ring. By mapping the observed shielding and deshielding zones onto the p22HBP structure, we estimated the position of the tetrapyrrole ring. Using this initial location for the bound PPIX, the ring current effect on p22HBP chemical shifts was calculated using the program SHIFTS-4.1 (32). We manually optimized the position of the PPIX ring to minimize the differences between the calculated ring current shifts and the experimental (p22HBP versus p22HBP-PPIX) chemical shift differences.

Experimental and calculated shift differences are compared in Fig. 5a, where it can be seen that there is very good agreement for most residues. Large deviations (>0.2 ppm) remained for a few residues, including 139, 171, and 179. Because conformational changes may accompany ligand binding and these residues are located in poorly defined loop regions, they were excluded from the final steps of the modeling process. The final model (Fig. 5b) positions the tetrapyrrole ring on the same surface (Fig. 5c) initially identified by chemical shift mapping (Fig. 4c), which also corresponds to the hydrophobic cleft observed in the free p22HBP structure (Fig. 3c).

Functional Homologs of p22HBP—A BLAST search using the murine p22HBP sequence identified a large number of putative members of the SOUL/p22HBP family, including animal, plant, and bacterial species (Fig. 6). Within the previously described HBP family, murine p22HBP is $>80\%$ identical to its mammalian orthologs, and sequence similarities decline to $\sim 30\%$ for the more distant relatives from *Arabidopsis* and *Rhodospseudomonas*. Interestingly, the p22HBP paralog murine SOUL is also relatively dissimilar, with 27% identity.

To assess whether p22HBP homologs are likely to bind tetrapyrrole ligands in an analogous manner, we generated a series of structural models using the p22HBP NMR structure as a template. Not surprisingly, models for the mammalian HBPs displayed a hydrophobic patch in exactly the same area as p22HBP, because residues throughout the α_A helix are highly conserved. Similar hydrophobic patches were more difficult to discern in models of HBPs from other species; however, absolutely conserved residues like Ala-54, Tyr-65, and Tyr-171 and other highly conserved apolar amino acids may preserve the same ligand binding site throughout the SOUL/HBP family.

Murine SOUL reportedly binds heme at a site that includes a histidine residue (His-42) (8). The model and electrostatic surface calculated for murine SOUL reveal a small hydrophobic patch similar to the cleft on p22HBP that binds heme and PPIX. However, the position corresponding to His-42 (Ala-35 in p22HBP) is far from this site, suggesting that SOUL binds heme in a manner altogether distinct from p22HBP.

DISCUSSION

We determined the NMR structure of murine p22HBP, the first structure of a protein from the SOUL heme-binding protein family (Pfam PF04832). Unanticipated structural similarity was found between the p22HBP structure and three bacterial proteins with $<10\%$ sequence identity. Of the three structural homologs, BmrR is a ligand-binding domain of a transcription activator, Rob is a transcription factor, and SbmC/GyrI/YeeB inhibits DNA gyrase. By analogy with these structural homologs, p22HBP might be considered a potential heme-activated regulator of gene expression or DNA replication. However, to participate directly in transcriptional regulation, p22HBP would need to be present within the nucleus, and previous subcellular localization studies using a green fluorescent protein fusion protein appear to suggest that p22HBP is restricted to the cytoplasm (3). Moreover, p22HBP is comprised of a single domain, whereas BmrR and Rob each contain distinct DNA binding domains in addition to an HBP/SOUL domain. Thus, the possibility that p22HBP functions in the nucleus to regulate gene expression seems remote.

Analysis of the NMR structure of murine p22HBP in conjunction with chemical shift changes upon tetrapyrrole binding indicates that a hydrophobic surface is responsible for interactions with heme and PPIX. This binding site does not correspond to a hydrophobic sequence (residues 73–82), originally identified as a likely binding determinant (4).

We measured equilibrium dissociation constants for these ligands in the 0.5–5 nM range. Our results coincide with the low nanomolar K_d values reported by Taketani *et al.* (4) for p22HBP-PPIX binding, in contrast to studies that reported K_d values of 0.9 μM and 11.5 μM for binding of heme and PPIX, respectively, to murine p22HBP (3) or 20 μM for the p22HBP-heme complex (8). The results presented in this work ought to

Solution Structure of p22HBP

be comparable with the work of Blackmon *et al.* (3), because the same protein and experimental method were used. However, there is a 10^{-3} discrepancy between K_d values. Blackmon *et al.* used high concentrations of p22HBP protein (receptor), which may have unintentionally biased the resulting K_d values, whereas we used low nanomolar protein concentrations and analyzed the binding data by non-linear fitting using a model that accounts for ligand depletion at high receptor concentration.

Previous studies concluded from optical and EPR spectroscopic measurements that iron coordination is unchanged upon hemin binding to p22HBP (3, 8). Our results are consistent with those results in that the ligand binding site contains no histidine residues. The structural results, combined with our observation that hemin binds with 6-fold lower affinity than PPIX can be taken as further confirmation that specific coordination of the iron by p22HBP does not accompany hemin binding.

The biological function of p22HBP remains undefined, but the protein is thought to bind excess heme in the cytosol to facilitate transport out of the mitochondria and perhaps as a buffer or sensor of available heme levels (34). p22HBP is expressed at high levels in the liver and induced during erythroid differentiation, where heme production is correlated with p22HBP expression levels (4). Mitochondrial heme needs to be transported and ultimately delivered to sites of hemoprotein synthesis, *i.e.* the cytoplasm or endoplasmic reticulum, but free heme is a feedback inhibitor of 5-aminolevulinic acid synthase (35). However, inhibition of ALAS by free heme may be undesirable in erythroid and hepatic cells, where heme synthesis is most active. p22HBP may therefore allow heme transported from the mitochondria to be sequestered in the cytosol while awaiting incorporation into newly synthesized hemoproteins. However, as the function of p22HBP remains undefined, it is unknown whether heme or hemin binds to, or is delivered to, p22HBP. It is therefore premature to assign the heme Fe electronic state in the cytosol at the time of binding to p22HBP.

Our studies have elucidated the structural basis for tetrapyrrole binding previously described for p22HBP. However, an entirely distinct biological activity has recently been attributed to the p22HBP polypeptide (6). Specifically, residues 1–21 of porcine HBP were found to function as a chemoattractant peptide for dendritic cells and monocytes. The porcine HBP N-terminal fragment isolated from spleen, termed F2L, is a potent agonist for FPRL2, a member of the formyl peptide receptor (FPR) family. The FPRs are G protein-coupled receptors that direct migration of leukocytes early in the immune response to bacterial pathogens.

No details on structure-activity relationships for F2L have been reported, so it is not known whether the entire HBP-(1–21) fragment is required for potent activation of the FPRL2 receptor. Nor is it known how or where processing of the expressed form of HBP occurs. However, it is interesting to note that murine p22HBP was originally isolated in a processed form corresponding to residues 7–190 (4), and this is the species that was produced recombinantly for structural and ligand binding studies presented here. Furthermore, residues 7–17 are disordered in the NMR structure and residues 18–23 form a

β -strand that is not present in structural homologs of p22HBP (Fig. 3) or conserved beyond the mammalian orthologs (Fig. 6). It is therefore conceivable that cleavage of HBP after Leu-21 would yield both a functional F2L ligand and a p22HBP protein that remains folded and competent for ligand binding. Nevertheless, additional work is needed to define the mechanism by which HBP protein is trafficked and processed, as well as the relationship between its divergent dual roles in heme metabolism and immune signaling.

The SOUL heme-binding proteins are ubiquitous in nature, with bacterial, archaeal, and eukaryotic representatives. We have determined the first structure of a protein from the SOUL/HBP family, murine p22HBP, measured its affinity for hemin and protoporphyrin-IX, and identified the heme binding site by NMR chemical shift mapping. The ligand binding site is composed of a hydrophobic cleft flanked by the α_A helix and the β_8 - β_9 loop. Our future studies will be directed at the experimental structure determination of a p22HBP-tetrapyrrole complex and structure-function investigations of other SOUL/HBP proteins.

Acknowledgment—B. J. G. thanks Dr. G. Pintacuda for the Mathematica (Wolfram Research, Inc.) script used to generate the inset in Fig. 5a.

REFERENCES

1. Goodfellow, B. J., Dias, J. S., Ferreira, G. C., Henklein, P., Wray, V., and Macedo, A. L. (2001) *FEBS Lett.* **505**, 325–331
2. Munakata, H., Sun, J. Y., Yoshida, K., Nakatani, T., Honda, E., Hayakawa, S., Furuyama, K., and Hayashi, N. (2004) *J. Biochem.* **136**, 233–238
3. Blackmon, B. J., Dailey, T. A., Lianchun, X., and Dailey, H. A. (2002) *Arch. Biochem. Biophys.* **407**, 196–201
4. Taketani, S., Adachi, Y., Kohno, H., Ikehara, S., Tokunaga, R., and Ishii, T. (1998) *J. Biol. Chem.* **273**, 31388–31394
5. Babusiak, M., Man, P., Sutak, R., Petrak, J., and Vyoral, D. (2005) *Proteomics* **5**, 340–350
6. Migeotte, I., Riboldi, E., Franssen, J. D., Gregoire, F., Loison, C., Wittamer, V., Dethoux, M., Robberecht, P., Costagliola, S., Vassart, G., Sozzani, S., Parmentier, M., and Communi, D. (2005) *J. Exp. Med.* **201**, 83–93
7. Zylka, M. J., and Reppert, S. M. (1999) *Brain Res.* **74**, 175–181
8. Sato, E., Sagami, I., Uchida, T., Sato, A., Kitagawa, T., Igarashi, J., and Shimizu, T. (2004) *Biochemistry* **43**, 14189–14198
9. Dias, J. S., Macedo, A. L., Ferreira, G. C., Jeanty, N., Taketani, S., Goodfellow, B. J., Peterson, F. C., and Volkman, B. F. (2005) *J. Biomol. NMR* **32**, 338
10. Smith, P. K., Krohn, R. I., Hermanson, G. T., Mallia, A. K., Gartner, F. H., Provenzano, M. D., Fujimoto, E. K., Goeke, N. M., Olson, B. J., and Klenk, D. C. (1985) *Analyt. Biochem.* **150**, 76–85
11. Swillens, S. (1995) *Mol. Pharmacol.* **47**, 1197–1203
12. Delaglio, F., Grzesiek, S., Vuister, G. W., Zhu, G., Pfeifer, J., and Bax, A. (1995) *J. Biomol. NMR* **6**, 277–293
13. Keller, R. (2004) *The Computer Aided Resonance Assignment Tutorial*, Cantina Verlag, Goldau, Switzerland
14. Bartels, C., Xia, T.-H., Billeter, M., Güntert, P., and Wüthrich, K. (1995) *J. Biomol. NMR* **5**, 1–10
15. Wishart, D. S., Bigam, C. G., Yao, J., Abildgaard, F., Dyson, H. J., Oldfield, E., Markley, J. L., and Sykes, B. D. (1995) *J. Biomol. NMR* **6**, 135–140
16. Cornilescu, G., Delaglio, F., and Bax, A. (1999) *J. Biomol. NMR* **13**, 289–302
17. Herrmann, T., Güntert, P., and Wüthrich, K. (2002) *J. Mol. Biol.* **319**, 209–227
18. Linge, J. P., Williams, M. A., Spronk, C. A., Bonvin, A. M., and Nilges, M. (2003) *Proteins* **50**, 496–506
19. Schwieters, C. D., Kuszewski, J. J., Tjandra, N., and Clore, G. M. (2003) *J.*

- Magn. Reson.* **160**, 65–73
20. Laskowski, R. A., Rullmann, J. A., MacArthur, M. W., Kaptein, R., and Thornton, J. M. (1996) *J. Biomol. NMR* **8**, 477–486
 21. Altschul, S. F., Madden, T. L., Schaffer, A. A., Zhang, J. H., Zhang, Z., Miller, W., and Lipman, D. J. (1997) *Nucleic Acids Res.* **25**, 3389–3402
 22. Gibrat, J. F., Madej, T., and Bryant, S. H. (1996) *Curr. Opin. Struct. Biol.* **6**, 377–385
 23. Ye, Y., and Godzik, A. (2003) *Bioinformatics* **19**, Suppl. 2, ii246–ii255
 24. Baker, N. A., Sept, D., Joseph, S., Holst, M. J., and McCammon, J. A. (2001) *Proc. Natl. Acad. Sci. U. S. A.* **98**, 10037–10041
 25. Dolinsky, T. J., Nielsen, J. E., McCammon, J. A., and Baker, N. A. (2004) *Nucleic Acids Res.* **32**, W665–W667 (web server issue)
 26. Marti-Renom, M. A., Stuart, A. C., Fiser, A., Sanchez, R., Melo, F., and Sali, A. (2000) *Annu. Rev. Biophys. Biomol. Struct.* **29**, 291–325
 27. Romanowski, M. J., Gibney, S. A., and Burley, S. K. (2002) *Proteins* **47**, 403–407
 28. Kwon, H. J., Bennik, M. H., Demple, B., and Ellenberger, T. (2000) *Nat. Struct. Biol.* **7**, 424–430
 29. Zheleznova, E. E., Markham, P. N., Neyfakh, A. A., and Brennan, R. G. (1999) *Cell* **96**, 353–362
 30. Newberry, K. J., and Brennan, R. G. (2004) *J. Biol. Chem.* **279**, 20356–20362
 31. Wuthrich, K., Shulman, R. G., and Yamane, T. (1968) *Proc. Natl. Acad. Sci. U. S. A.* **61**, 1199–1206
 32. Xu, X. P., and Case, D. A. (2001) *J. Biomol. NMR* **21**, 321–333
 33. Bertini, I., Luchinat, C., Parigi, G., and Pierattelli, R. (2005) *ChemBiochem* **6**, 1536–1549
 34. Latunde-Dada, G. O., Simpson, R. J., and McKie, A. T. (2006) *Trends Biochem. Sci.* **31**, 182–188
 35. Lathrop, J. T., and Timko, M. P. (1993) *Science* **259**, 522–525
 36. Notredame, C., Higgins, D. G., and Heringa, J. (2000) *J. Mol. Biol.* **302**, 205–217